Mean flows and blob velocities in scrape-off layer (SOLT) simulations of an L-mode discharge on Alcator C-Mod

D. A. Russell, J. R. Myra and D. A. D'Ippolito
Lodestar Research Corporation

B. LaBombard, J. W. Hughes and J. L. Terry
Plasma Science and Fusion Center, Massachusetts Institute of Technology

S. J. Zweben
Princeton Plasma Physics Laboratory

April 2016

submitted to *Physics of Plasmas*

DOE/ER/PPPL/S013429-U-1, ER/54392-81 LRC-16-165

LODESTAR RESEARCH CORPORATION
2400 Central Avenue
Boulder, Colorado 80301

Mean flows and blob velocities in scrape-off layer (SOLT) simulations of an L-mode discharge on Alcator C-Mod

D. A. Russell,† J. R. Myra and D. A. D'Ippolito
Lodestar Research Corporation, 2400 Central Ave., P-5, Boulder CO 80301, USA

B. LaBombard, J. W. Hughes and J. L. Terry
Plasma Science and Fusion Center, Massachusetts Institute of Technology, 167 Albany Street, Cambridge, Massachusetts 02138, USA

S. J. Zweben
Princeton Plasma Physics Laboratory, P.O. Box 451, Princeton NJ 08540, USA

PACS numbers: 52.35.Ra, 52.40.Kh, 52.55.Fa, 52.65.Kj

Abstract

Two-dimensional scrape-off layer turbulence (SOLT) code simulations are compared with an L-mode discharge on the Alcator C-Mod tokamak [M. Greenwald, et al., Phys. Plasmas **21**, 110501 (2014)]. Density and temperature profiles for the simulations were obtained by smoothly fitting Thomson scattering and mirror Langmuir probe (MLP) data from the shot. Simulations differing in turbulence intensity were obtained by varying a dissipation parameter. Mean flow profiles and density fluctuation amplitudes are consistent with those measured by MLP in the experiment and with a Fourier space diagnostic designed to measure poloidal phase velocity. Blob velocities in the simulations were determined from the correlation function for density fluctuations, as in the analysis of gas-puff-imaging (GPI) blobs in the experiment. In the *simulations*, it was found that larger blobs moved poloidally with the ExB flow velocity, v_E , in the near-SOL, while smaller fluctuations moved with the group velocity of the dominant linear (interchange) mode, $v_E + 1/2\ v_{di}$, where v_{di} is the ion diamagnetic drift velocity. Comparisons are made with the *measured* GPI correlation velocity for the discharge. The saturation mechanisms operative in the simulation of the discharge are also discussed. It is found that neither sheared flow nor pressure gradient modification can be excluded as saturation mechanisms.

†email: **dave@lodestar.com**

I. Introduction

Flows are ubiquitous in edge and scrape-off-layer (SOL) tokamak plasmas; understanding their origin and effects on plasma turbulence and transport has been a topic of interest for many years. Sheared E×B flows, in particular, are believed to be important in this respect.[1,2] Efforts to understand the low (L) mode to high (H) mode confinement transition in tokamaks have further increased interest in this topic.[3-11] A closely related subject is that of understanding the saturation mechanism for edge and SOL turbulence.[12,13] In addition to contributing to L-H mode transition physics, some models predict that turbulence in the vicinity of the separatrix could be sufficiently large so as to impact the width of the heat flux channel.[14-21]

Binormal (approximately poloidal) flows that vary in the radial direction are routinely observed in the outer midplane region of tokamaks as for example in Refs. 22-24. Often, such flows are not measured directly, but rather inferred from measurements of the radial electric field E_r (allowing calculation of the poloidal E×B drift $v_{E\theta}$), the density or pressure profiles (for the diamagnetic drifts), or from velocimetry of imaging diagnostics such as gas puff imaging (GPI).[25,26] In the latter case the flow speeds *of turbulent structures* can be deduced by time-delay estimation (TDE) methods, of which there are several variants,[22,27,28] Fourier (phase velocity) methods,[29] or by algorithms which track the locations of the structures in time.[30,31] There can be significant differences in the results of these different types of diagnostic measurements and analysis methods, and sometimes subtle differences in their interpretation.[32]

Turbulence in the edge and SOL frequently takes the form of coherent structures, often referred to as blobs or blob filaments.[33,34] From the standpoint of both theory and experimental interpretation, it is important to understand the relationship between the binormal (poloidal) velocity of the blob structures and the flow velocity of the background plasma (e.g. time averaged) on which they propagate. In what situations do these turbulent structures propagate at

the phase or group velocity associated with underlying linear modes? In what situations do the velocity of the blobs constitute the background flow itself, or follow this flow?

In this paper, we will explore such questions for a well diagnosed discharge in the Alcator C-Mod tokamak[35] using reduced model simulations carried out with the scrape-off layer turbulence (SOLT) code.[36] Our investigations, which include comparison of code results to experimental ones, are made possible by the existence of both high quality GPI data and plasma profile data.

The GPI data is obtained from the discharge by two different methods. Briefly, a small amount of neutral helium gas is puffed in at the plasma edge, and the resulting light emission is imaged by a fast framing-rate "Phantom" camera,[22] and onto an avalanche photo-diode (APD) array,[28] in a plane which is approximately perpendicular to the local magnetic field. Since the emission depends on the local density and temperature, which have turbulent fluctuations, the turbulence structures can be visualized. In the present paper, Fourier analysis (FA) has been applied to both the Phantom camera and the APD-array images to yield radial profiles of poloidal phase velocities of the fluctuations in the outboard midplane region, and TDE analysis has been applied to the APD images to yield both poloidal and radial phase velocity profiles of the fluctuations.

The plasma profile data in the SOL and near-edge (closed surface) region is taken with a mirror Langmuir probe (MLP) diagnostic recently installed on Alcator C-Mod, and described in detail in Ref. 24. This diagnostic yields extremely high quality time resolved data for plasma potential, density and electron temperature. It is combined with Thomson scattering data for density and electron temperature deeper into the edge region to provide plasma profile coverage for the entire region of interest. This multiple-probe head MLP system also provides a TDE measurement of fluctuation poloidal velocities and a measurement of fluctuation amplitudes.

In the present paper, as described in detail in the following, we will use the time-averaged "background" plasma profiles as input for the simulations. The SOLT code simulation results

for the turbulence will then be compared with GPI and MLP fluctuation measurements. We will compare calculated background E×B, diamagnetic drift and phase velocities for the measured profiles with those of the simulation and compare the simulation and experimental results for the binormal (or poloidal) velocity of the turbulent structures. The results from using several algorithms for deducing the latter from simulation and experimental data will also be compared.

The plan of our paper is as follows. In Sec. II the simulation model, evolution equations and input parameters and profiles are presented. Simulation results are given in Sec. III for the fluctuation amplitudes, mean flows, and blob velocities, with a comparison of GPI and simulation results. Turbulence saturation mechanisms are investigated in Sec. IV: wave breaking or profile modification, and stabilization by flow shear. Finally, our conclusions are given in Sec. V.

II. The simulation model

A. Equations of evolution

The SOLT model equations have been elucidated previously. Here we briefly recapitulate the description given in Ref. [17] for completeness. Our choice of parameters and profiles for simulating the L-mode discharge is described in Sec. II.B.

The SOLT code models the evolution of four fields: electrostatic potential, density and temperatures (electron and ion) in a plane perpendicular to the magnetic field **B** in the outboard midplane (OM) region of the tokamak. The simulation plane is the (x,y) plane in a Cartesian space where x, y, and z are respectively the radial, binormal (approximately poloidal), and parallel (to **B**) coordinates. The potential is obtained from a generalized vorticity. SOLT includes a reduced description of the electron drift wave and interchange instabilities, and sheath physics. Curvature- and ∇B-driven charge polarization enables transport of enhanced density

structures (blobs) with strong fluctuations ($\tilde{n}/n \sim 1$) from the edge into the SOL. The parallel physics is modeled by closure schemes that depend upon the collisionality regime.[33] Other important features of the model are that (i) it does not use the Boussinesq approximation, and (ii) it retains ion temperature effects ($T_i \neq 0$). The first feature is important for properly treating transport in regions of high density gradient such as the edge region and blob boundary.[37] The second point is important as warm ions, which are expected to be present in the edge and SOL region,[38,39] influence the dynamics of turbulence and blob propagation.[40-45] The underlying linear normal mode of interest in the present simulations is the interchange mode, importantly modified by the finite ion temperature (cf. Sec. III.B).

In dimensionless form, the SOLT model equations are

$$(\partial_t + \mathbf{v}_E \cdot \nabla)\rho = -2\mathbf{b} \times \kappa \cdot \nabla(p_e + p_i) - \alpha_{sh} J_{||} - A_{dw}(\Phi, n) + \mu \nabla^2 \rho + \frac{1}{2} n \mathbf{v}_{di} \cdot \nabla \nabla^2 \Phi + \frac{1}{2} \nabla^2 (\mathbf{v}_E \cdot \nabla p_i) - \frac{1}{2} (\mathbf{v}_E \cdot \nabla) \nabla^2 p_i + \frac{1}{2} \mathbf{b} \cdot \nabla v_E^2 \times \nabla n \tag{1}$$

$$(\partial_t + \mathbf{v}_E \cdot \nabla) n = -\alpha_{sh} \Gamma_{||e} + A_{dw}(\Phi, n) + D_n \nabla^2 n + S_n \tag{2}$$

$$(\partial_t + \mathbf{v}_E \cdot \nabla) T_e = -\alpha_{sh} q_{||e} / n + D_{Te} \nabla^2 T_e + S_{Te} \tag{3}$$

$$(\partial_t + \mathbf{v}_E \cdot \nabla) T_i = -\alpha_{sh} q_{||i} / n + D_{Ti} \nabla^2 T_i + S_{Ti} \tag{4}$$

where the generalized vorticity ρ evolved in Eq. (1) is defined by

$$\rho = -\nabla \cdot (n \nabla \Phi + \nabla p_i) \tag{5}$$

The equations are written in dimensionless form using Bohm normalization with reference time-scale $\Omega_{ci}^{-1} = (ZeB/m_i c)^{-1}$ and space-scale $\rho_{sr} = c_{sr}/\Omega_{ci}$, where $c_{sr}^2 = T_{er}/m_i$, and T_{er} is a reference temperature for the normalization. Φ is the electrostatic potential, n is the electron density, $T_{e,i}$ are the electron and ion temperatures, and $p_{e,i} = n\, T_{e,i}$ are the corresponding pressures. The $\mathbf{E}\times\mathbf{B}$ velocity is $\mathbf{v}_E = \mathbf{b} \times\nabla\Phi$, where $\mathbf{b}$ is a unit vector in the magnetic field direction, perpendicular to the plane of the simulations. The ion diamagnetic drift velocity is $\mathbf{v}_{di} = \mathbf{b} \times\nabla p_i/n$.

The SOLT code evolves the ion pressure and the generalized vorticity defined in Eq. (5), thus dynamically coupling the ion diamagnetic and E×B drifts. The vorticity evolution (1) is consistent with the drift-ordered, reduced-Braginskii fluid model version derived by Simakov and Catto[46] and is also used in the BOUT code.[47]

The curvature and grad-B forces combine in the first term ($\sim \kappa \equiv \mathbf{b}\cdot\nabla b$) on the right-hand side of Eq. (1) to drive the interchange instability. In our coordinate system, this term is simply $\beta\, \partial_y(p_e+p_i)$, where $\beta = 2\rho_{sr}/R$ and R is the radius of curvature of the magnetic field ($1/\kappa$), here approximated by the (low field side) major radius of the tokamak. The linearized equations recover the interchange growth rate, $\gamma_{mhd}^2 = -\beta\partial_x(p_e + p_i)$.

The current density $J_{||}$, electron particle flux $\Gamma_{||e}$ and heat fluxes $q_{||e,i}$ in Eqs. (1) - (4) close the system of equations when expressed in terms of Φ, n, T_e and T_i. Those closure relations, valid for a range of collisionality regimes, from conduction-limited (at high collisionality) to sheath-connected, are discussed at greater length in the literature.[14,17] The

current and heat flux adjust continuously between sheath- and conduction-limited expressions in the SOL as the fields evolve, depending self-consistently on the character of the turbulence. Terms proportional to $\alpha_{sh}(x)$ describe losses to the sheath in various collisionality regimes. The operator A_{dw}, which is proportional to a coefficient α_{dw}, is a model drift-wave operator. See Appendix A of reference [17] for the complete form of these expressions.

The equilibrium profiles vary in the x (radial) dimension in the simulations. The core-side boundary is at x = 0, the separatrix is at $x = L_x/2$, and the far-SOL boundary is located at $x = L_x$ where L_x is the length of the radial domain. We also define a local radial coordinate $\Delta x = x - L_x/2$ such that the separatrix is located at $\Delta x = 0$. The drift wave and sheath profiles, $\alpha_{dw}(x)$ and $\alpha_{sh}(x)$, define the "separatrix" in SOLT simulations. In the edge region ($\Delta x < 0$), $\alpha_{dw}(\Delta x) > 0$ and $\alpha_{sh}(\Delta x) = 0$: drift wave physics is modeled on closed filed lines. In the SOL region ($\Delta x > 0$), $\alpha_{sh}(\Delta x) > 0$ and $\alpha_{dw}(\Delta x) = 0$: the field lines terminate on sheaths. Thus the boundary between the drift-wave and sheath regions ($\Delta x = 0$) defines the "separatrix." The α_{dw} and α_{sh} profiles are shown in Fig. 1.

Explicit diffusion coefficients are μ, D_n, D_{Te} and D_{Ti}. These describe diffusive transport processes in addition to those generated self-consistently by drift-interchange turbulence, e.g. neoclassical transport, collisional transport processes due to neutrals, and instabilities outside the scope of the present model. (For example, short scale drift waves have been shown to result in secondary instability and turbulence that dissipates the blob as it propagates across the SOL.[48]) As it is difficult to extract appropriate values for these coefficients from experimental data, we regard them as "free" parameters and adjust them to achieve physically credible results: they

should dissipate the high-k turbulence but not be so large as to dominate the SOL heat flux width or turn off instability. In Sec. III, we describe adjusting the density diffusion coefficient D_n to tune the amplitude of the density fluctuations in the simulations.

The sources, S_n , S_{Te} , and S_{Ti} , have the form $S_n = \nu_n(n_0(x) - \bar{n})$, etc., where the over-bar indicates the y-average. The sources restore the mean profiles to the reference profiles ($n_0(x)$, etc.) taken from the experiment but do not act on the fluctuations. These "restorative" sources represent neutral ionization and plasma heating, for example, and also maintain profiles against fluctuations, born in the outboard midplane region, with plasma that streams in and out of the midplane region along the closed field lines.

All fluctuations vanish at both x-boundaries. (At the wall in the experiments, *relative* fluctuations, $\delta n / \bar{n}$ etc., are order unity, and the mean fields $\bar{n}$ and absolute fluctuations $|\delta n|$ approach zero.) In particular, the electrostatic potential is taken to be constant at both radial boundaries, and these conditions are used to solve Eq. (5) for the potential. The turbulence is homogeneous in the binormal (y) dimension (viz., time-averages are independent of y) where periodic boundary conditions are applied.

B. Parameters and profiles

Density and electron temperature reference profiles for the simulations, plotted in Fig. 1, are smooth fits to Thomson scattering (TS) and mirror Langmuir probe (MLP) data recorded for L-mode discharge #1120711021 at Alcator C-Mod. Theses profiles are used in the source functions in Eqs. (2) and (3), and the simulation profiles, i.e., the y-averages of n(x,y,t) and T_e(x,y,t), tend to relax to them as described in Sec. II.A above. Time-averaged profiles from a

simulation, judged to be a good fit to the discharge, are plotted as discrete symbols in Fig. 1. The error bars represent the standard deviation with respect to time of the simulation profiles. It is apparent that the simulation profiles remain close to the reference profiles for the discharge.

Because ion temperature data is not available for the discharge, the ion temperature was taken to be a constant, throughout the simulation domain, equal to the reference electron temperature at the separatrix. Thus the ion pressure profile and fluctuations are simply proportional to those of the density.

The reference quantities used to express the dimensionless variables of Eqs. (1-5) in physical units are determined from the discharge data at the separatrix: the magnetic induction is 4.2 Tesla, $\Omega_{ci}/2\pi = 32$ MHz; $T_{er} = 48.5$ eV, $\rho_{sr} = 0.24$ mm and $c_{sr} = 48.2$ km/sec; the curvature drive (cf. Sec. II.A) $\beta = 2\rho_{sr}/R = 5.54\times10^{-4}$ (R = 86.6 cm), and this is a deuterium plasma.

The connection length, $L_{//}(x)$, is obtained from the MHD equilibrium code EFIT, and we linearly interpolate its reciprocal onto the simulation grid as the sheath absorption (or conductivity) coefficient, $\alpha_{sh} = 2\rho_{sr} / L_{//}(x)$, which is plotted in Fig. 1. The sudden increase in α_{sh} at $x \cong 1.3$ cm corresponds to the shadow of a limiter at C-Mod.

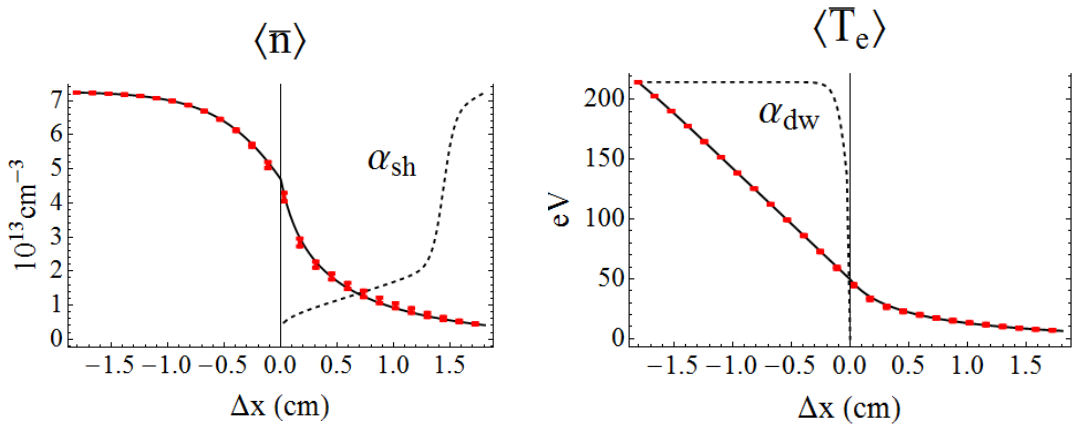

Fig. 1. Time-averaged density and temperature profiles from a simulation (D_n = 0.04 m^2/sec) plotted as discrete points (red). The height of the point symbol is the standard deviation with respect to time, seen to be negligible on the scale of the plot. Also plotted are the reference density and electron temperature profiles (solid) for the discharge, and the sheath (α_{sh}) and drift wave (α_{dw}) coefficients (dashed), rescaled to fit the plot. The over-bar denotes the y-average, and the angular brackets denote the time-average.

The drift wave coefficient, $\alpha_{dw}(x) = (1 - \tanh(x-x_0)/\Delta) \times 2\rho_{sr}^2\Omega_e /(L_{//e}^2\nu_{ei0})$, decreases rapidly as the edge is approached from the core side, reflecting the increase in field line length due to the X-point, the drop in T_e and the corresponding rise in collisionality. The electron-ion collision rate, ν_{ei0}, is calculated for reference parameters at the separatrix, and we take $1/k_{||} \sim L_{//e} \sim qR$ with local "safety factor" $q \sim rB/RB_\theta = 3.5$, $\Delta = 5\ \rho_{sr}$ and $x_0 = 10\ \rho_{sr}$. The drift wave coefficient is plotted in Fig. 1. Notice that the drift wave coefficient vanishes for $\Delta x > 0$; we do not model drift waves on the open magnetic field lines.

Dissipation parameters acting on the fluctuations are not experimentally determined for the discharge, so we take them to be adjustable in the simulations in order to explore dependencies of the results on the amplitude of the turbulent fluctuations. (See the discussion in

Sec. II.A.) In the work reported here, all dissipation parameters are held fixed ($\mu = 0.1$, $D_{Te} = 0.02$) except the density diffusion coefficient D_n which is varied to provide a range of fluctuation amplitudes.

The relaxation rates used in the density and temperature sources are constant throughout the simulation domain: $\nu_n = \nu_{Te} = 0.01$. This differs from our previous simulations[15] of an EDA H-mode on C-Mod in which the restorative dynamics did *not* act in the SOL, and our focus was on determining the heat flux width in the near-SOL due to turbulent fluctuations driven by profiles prescribed *only* in the edge region ($\Delta x < 0$) but free to evolve in the SOL. Here our emphasis is on determining the nature of fluctuations (viz., blob velocities) in the SOL that are consistent with the measured profiles in the SOL as well as in the edge region. We emphasize that in both cases the *fluctuations* were *not* subjected to the restorative dynamics enforced by the sources in Eqs. (2-4).

III. Simulation results

A. Density fluctuations vs. Dn

As seen in Fig. 2(a), the amplitude of density fluctuations in the steady state decreases with increasing diffusion coefficient D_n. At the largest value of D_n, the turbulence consists of relatively weak quasi-linear fluctuations, shown in Fig. (3a), and may be below threshold for the interchange instability as a linear growth phase is not apparent at early times. At the second highest value of D_n, the instability is weakly excited, and, in the saturated state, the fluctuations are poloidally localized in radial streamers stretching from the edge to the limiter, shown in Fig. (3b). With decreasing D_n there is an abrupt transition, apparent in Fig.2(a), to a regime of

markedly larger fluctuations dominated by structures localized radially and poloidally (blobs) in the SOL, as seen in Fig. (3c).

The profile of the density fluctuation amplitude for the "blobby" simulation, with D_n = 0.04 m^2 /sec, is plotted in Fig. 2(b). The MLP data indicates a fluctuation amplitude of $\delta n/n \sim$ 20% at the separatrix ($\Delta x = 0$) for the discharge. Since $\delta n/n$ reaches 20% within 0.2 cm of the separatrix, and because it is blobby, like the discharge, this simulation was chosen as a good match to the discharge for the purpose of comparing blob velocities in Sec. III.D. The value of the diffusion coefficient in this "best-match" case is on the order of that typically inferred for C-Mod experimental analysis of particle transport at the separatrix, but less than that inferred in the far-SOL.[49] This is to be expected if density transport arises primarily from turbulence (including blobby turbulent convection) rather than directly from D_n in SOLT.

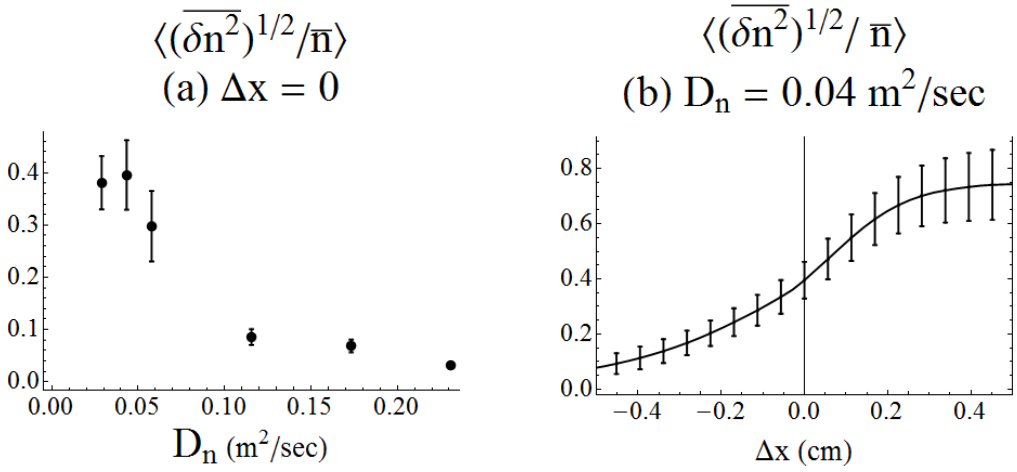

Fig. 2. Relative density fluctuation: the time-averaged r.m.s. density fluctuation, with respect to y, divided by the y-averaged density, in the simulations, (a) measured at the separatrix, versus the density diffusion coefficient D_n, and (b) versus radius (Δx) for D_n = 0.04 m^2/sec. The over-bar denotes the y-average; the angular brackets denote the time-average; error bars are standard deviations with respect to time, and the sample was restricted to the steady state in each case.

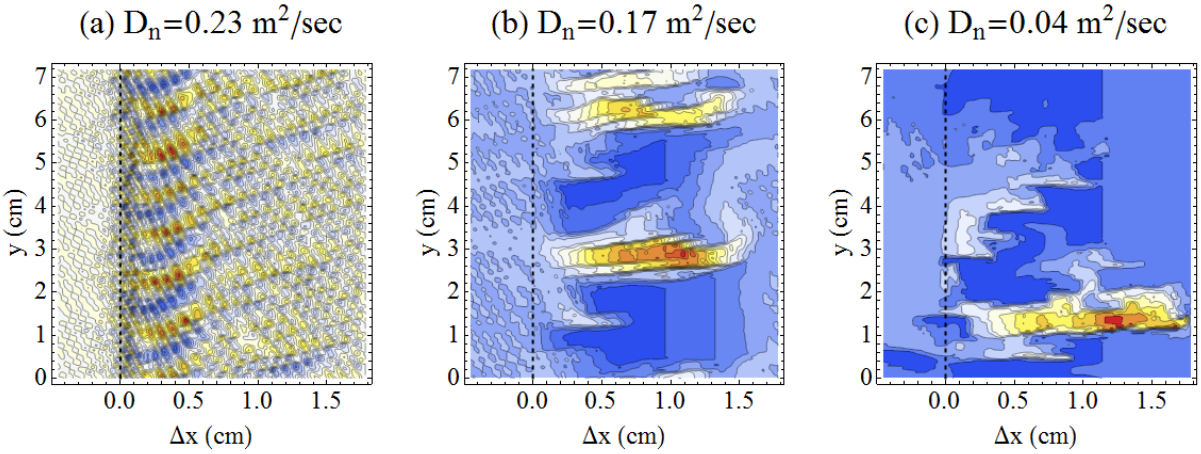

Fig. 3. Snapshots of the instantaneous density fluctuation divided by the y-averaged density, $(n-\bar{n})/\bar{n}$ from the simulations for (a) D_n = 0.23 m^2/sec, in the weak-turbulence, possibly sub-threshold, regime, (b) D_n = 0.17 m^2/sec, over threshold, where streamers are observed, and (c) D_n = 0.04 m^2/sec, in the strong turbulence regime where isolated blobs are observed in the SOL.

B. Mean flows

The mean flows of interest in this study are (1) the y-component of the ExB velocity, $\bar{v}_{E,y} = \partial_x \bar{\Phi}$, or simply v_E, where the mean, viz. y-average, is denoted by the over-bar, (2) the y-component of the ion diamagnetic velocity, $\bar{v}_{di,y} = \langle \partial_x p_i / n \rangle_y$, or simply v_{di}, and (3) the group (and phase) velocity of the interchange mode, $v_g = v_E + v_{di}/2$, modified for $T_i > 0$.[50] Time-averages of these mean flows are plotted in Fig. 4. The broad negative minimum in v_E outside the separatrix is commonly observed in the simulations and is due to sheath physics: the sheath-

limited parallel current in the SOL works to maintain $\Phi = 3T_e$, the Bohm potential, and $T_e(\Delta x)$ is decreasing in the SOL.

The v_E profile measured by the MLP in the discharge is plotted in Fig. 4(b) with triangles. (The MLP v_E profile appears to line up better with the simulation v_{di} profile, though this is likely fortuitous.) Both profiles have a broad minimum in the SOL, with the MLP minimum located about 2 mm closer to the separatrix and at ~ ¾ of the simulation minimum value. The disparity between the experimental and simulated v_E profiles reflects a disparity in the electrostatic potentials. (The potential is *not* subjected to restoration to a prescribed profile in the simulation, as are the density and the electron temperature profiles, but "freely" evolves according to Eqs. (1) and (5).) The differences between the potentials may be attributed to SOLT's (2D) reduced model of the (3D) parallel physics ($J_{//}$,$\Gamma_{//}$,$q_{//}$), as it affects the evolution of fluctuations that determine the potential. But the agreement between MLP and SOLT v_E profiles would be improved by a 2 mm radial shift, consistent with experimental uncertainty in determining the location of the separatrix.

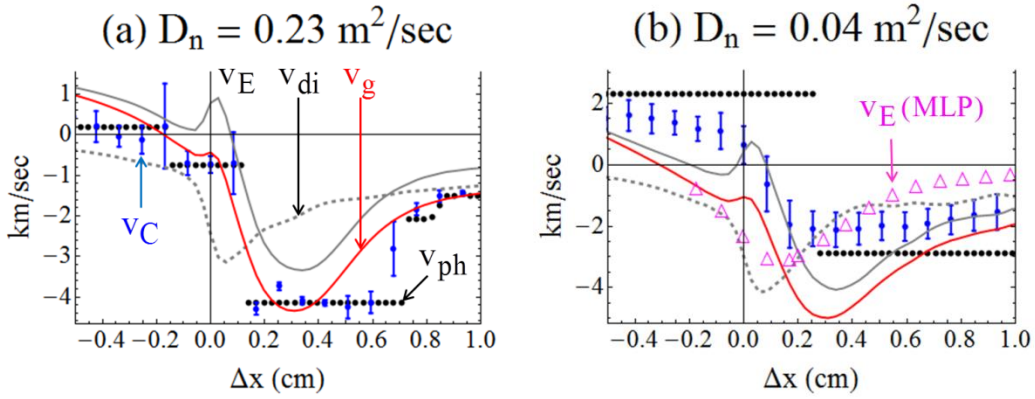

Fig. 4. Mean flow velocities in the binormal (y) direction: v_E (solid gey), v_{di} (dashed gray) and v_g (solid red) are plotted versus radius (Δx), along with the local phase velocity, $v_{ph} = \omega/k_y$, from Fourier analysis (black dots), and the correlation velocity, v_C (blue dots). In the v_C plot, the error bars are standard deviations with respect to the y-average. (a) $D_n = 0.23$ m^2/sec. (b) $D_n = 0.04$ m^2/sec. v_E measured by the MLP in the experiment is plotted with triangles in (b).

C. Blob velocities in the simulations

In a recent study comparing different GPI blob velocity diagnostics,[32] two measures received particular attention: one based on the Fourier transform of the fluctuations in the emission intensity, δI, and the other based on the correlation function of the intensity fluctuations. In this section we compare them in the context of the weak-turbulent and strong-blobby simulations. We take the density fluctuations in the simulations, ($\delta n = n - \bar{n}$), as a proxy for the intensity fluctuations in the GPI data.

C.1 Fourier phase velocity

The Fourier analysis (FA) method determines the y-components of the phase and group velocities of density fluctuations from the power spectrum, $\left|\delta n(x, k_y, \omega)\right|^2$. It is most useful in regimes where the fluctuations are relatively weak and the spectrum is narrow, e.g., dominated by a single wave. In the present work, we simply record the phase velocity, $v_{ph} = \omega / k_y$, at the maximum of the spectrum. v_{ph} is plotted in Fig. 4(a) for the weak-turbulence simulation with $D_n = 0.23$ m^2/sec, in which case it is constant on distinct radial zones and threaded by the phase (and group) velocity, v_g, of the interchange mode based on *local* linear analysis. This picture suggests that the generalization of the local analysis to the inhomogeneous setting of the

simulation would reveal radially localized interchange eigenmodes underlying the weak-turbulence fluctuations, as observed in previous studies of edge turbulence in Alcator C-Mod.[51]

Although the FA method is appealing for its simplicity, its usefulness as a measure of mean poloidal blob velocities is compromised in regimes of larger fluctuation amplitudes and broader spectra. In Fig. 4(b), v_{ph} is plotted for the simulation with $D_n = 0.04$ m^2/sec, for which big, blobby fluctuations dominate the SOL. It is constant on two radial zones, one emanating from the core and spanning the separatrix, and the other filling out the SOL. But movies of the fluctuations show a greater variety of blob bi-directional (poloidal) velocities than found by the v_{ph} measure in this regime, so a more articulate measure is required.

C.2 Correlation velocity

Time-delay estimation (TDE) methods are routinely used to track the motion of GPI blobs.[22,27,28] A particular version of the method[28] was applied to the GPI data recorded for the discharge and a similar method[22] to the density fluctuations in the simulations. The method used in the simulations tracks the displacement $(\delta x_m,\delta y_m)$ of maxima of the correlation function for density fluctuations, normalized by the r.m.s. fluctuation,

$$\frac{\left\langle \delta n(x,y,t)\cdot \delta n(x+\delta x,y+\delta y,t+\delta t)\right\rangle}{\left\langle \delta n(x,y,t)^2\right\rangle^{1/2}\left\langle \delta n(x+\delta x,y+\delta y,t)^2\right\rangle^{1/2}} \tag{6}$$

at each (x,y) and for a sequence of time (or frame) delays δt_m. (The angular brackets denote an average over time.) The vector, $\underline{v}_{C,m}(x,y)=(\delta x_m,\delta y_m)/\delta t_m$, defines the *correlation velocity* at (x,y) corresponding to the time delay δt_m.[22] At each (x,y), a sequence of sub-domains, $\{W_m\}$, of the simulation domain (or GPI window) are searched for correlation maxima, and the same window sequence is used for all (x,y). In order that maxima discovered for delay δt_m not escape detection for the larger delay δt_{m+1} it is necessary that the window size increase with the delay: $W_m / \delta t_m$ is a constant chosen large enough so that correlation maxima (δx_m , δy_m) lie within the window but small enough so that the largest window, centered on (x,y), lies within the simulation (or GPI) domain. Thus, for example, larger radial velocities, $\delta x_m/\delta t_m$, confine the analysis increasingly away from the radial (x) boundary: $x < L_x - \max(|\delta x_m|)$ in the simulations.

The y-component of the correlation velocity (v_C), averaged over time delays (δt = 0.5,1.0,1.5 and 2.0 μs) is plotted in Fig. 4 for two SOLT simulations. In the weak-turbulence

case, Fig. 4(a), the correlation velocity follows the phase velocity v_{ph} closely; both the FA and TDE methods find radially localized interchange modes. In the strong-turbulence case, Fig. 4(b), the two methods give somewhat different results, and neither one is particularly attracted to the linear interchange mode which is practically irrelevant to blob motion in this regime: in the near-SOL and edge regions, v_C closely follows v_E.

As mentioned in Sec. III.C.1, the FA method is expected to fail in strong-turbulence regimes. But the accord between the two methods in the weak-turbulence regime serves to verify both the FA and TDE methods used here.

D. GPI and simulation blob velocities compared

The blob velocities measured in the discharge and in the strong-turbulence simulation (D_n = 0.04 m^2/sec) are compared in Fig. 5. The bi-normal (~poloidal) components of the velocities determined by four different measurements of fluctuations observed in the discharge are compared in Fig. 5(a): 1) TDE analysis of GPI emission recorded by an avalanche photo-diode (APD) array, 2) FA of GPI emission recorded by the APD array, 3) FA of GPI emission recorded by the Phantom camera, and 4) 2-point phase-delay analysis of fluctuations measured by the MLP. These are plotted along with the correlation velocity profile for the simulation taken from Fig. 4(b). All are seen to be in good agreement in the SOL, while the measured velocities for the discharge are about a factor of three greater than the simulation velocities on the core side of the separatrix.

Both the discharge and simulation poloidal velocities change sign near the separatrix. In the simulation, the sign change is located where the skewness of the density fluctuations passes

through zero, i.e., in (or at) the blob " birth zone."[34] This "jump" in the poloidal velocity is also a persistent feature in the experimental data, found in the TDE and FA measurements of the velocity and in 2-point phase-delay analysis of the MLP data. In fact, the jump is used to align the GPI and MLP velocity profiles. This alignment is essential for comparing the GPI and simulation velocity profiles, since the later are driven by the MLP density and temperature profiles.

The radial components of the velocities are compared in Fig. 5(b) and are seen to be in good agreement. (Note that the FA method and the MLP were not used to determine *radial* velocity profiles.) In the simulation, the measurement is limited in radius so that the search window is contained within the radial domain, as discussed in Sec. III.C.2. Thus the larger radii explored in the experiment are not accessible in the simulations. (The bi-normal (y) velocity component is not so restricted because the simulations are periodic in y.)

Where it is positive, the relative density fluctuation is a good proxy for the GPI signal, i.e., for blobs. However, on the core side of the blob birth zone, the strongest correlations in the simulation are found for *holes* (viz. $\delta n < 0$), which have negative radial velocity, as seen in Fig. 5(b).

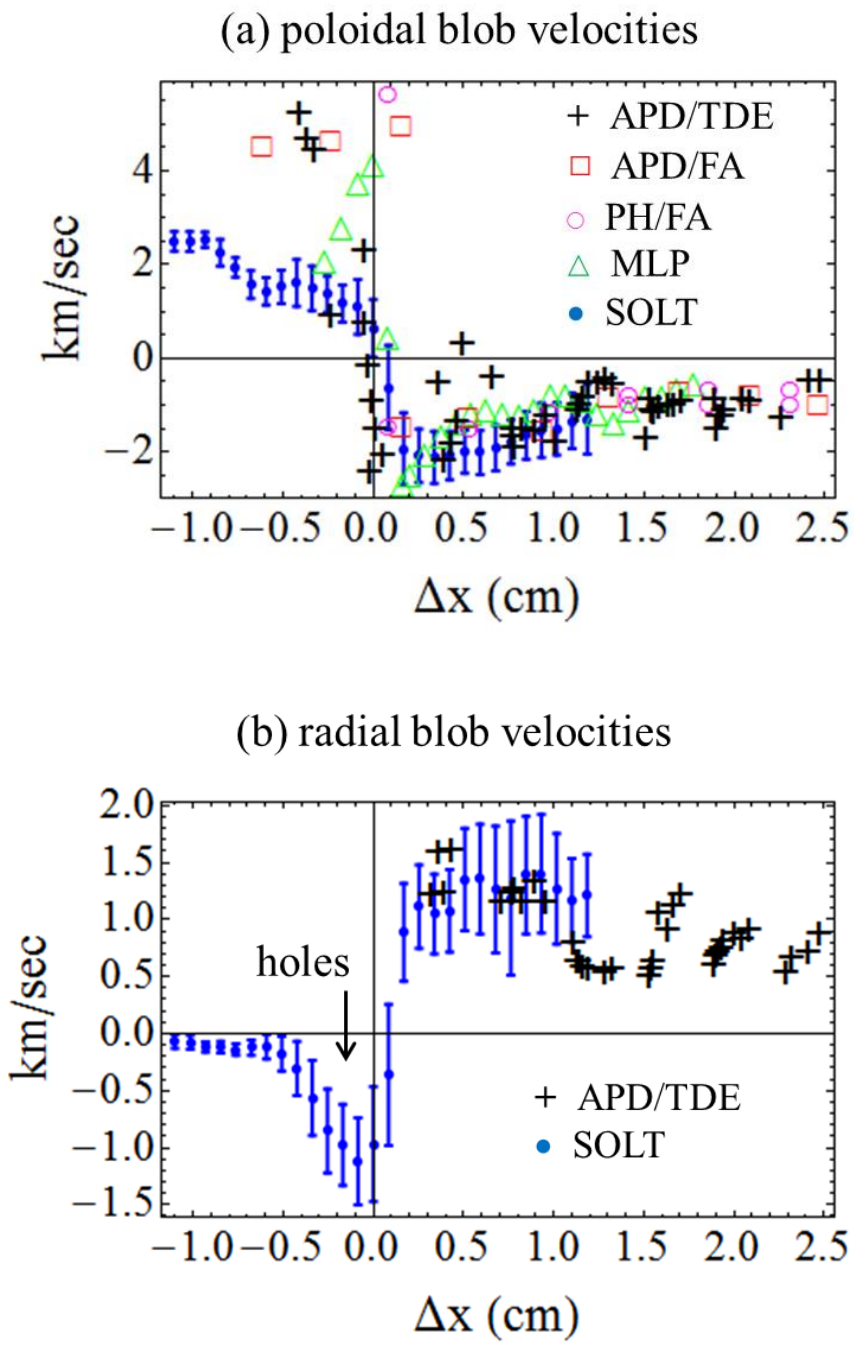

Fig. 5. Poloidal (a) and radial (b) components of the correlation velocity for the strong-blobby simulation (D_n = 0.04 m^2/sec) are plotted (dots with error bars) versus radius and compared with different measures of the corresponding velocity components of fluctuations in the discharge. In (a) and (b), (+) denotes time-delay estimation (TDE) analysis of GPI data captured by the avalanche photo-diode (APD) array. In (a), (□) denotes Fourier analysis (FA) of GPI data

captured by the APD array, (O) denotes FA of GPI data captured by the Phantom camera (PH), and (Δ) denotes 2-point phase-delay analysis of fluctuations measured by the MLP.

IV. Saturation mechanisms

A. Stabilization by sheared flow

It is well known that shear in the mean ExB flow can act to reduce the growth rate of the interchange instability[1] and thus provide a saturation mechanism for the instability if the shearing rate is comparable to the growth rate. In all of the simulations presented here, there is evidence that this saturation mechanism is at work.

For example, the simulation with D_n = 0.17 m^2/sec is evidently above threshold for the interchange instability. The early evolution of the density fluctuation in this case, starting from small-amplitude noise, is shown in Fig. 6(a) where initial growth and subsequent saturation, in the streamers of Fig. 3(b), are apparent. The corresponding histories of (a) the magnitudes of the extrema of the ExB flow shearing rate ($\xi_E = \partial_X \bar{v}_E$) and of (b) the maximum of the interchange growth rate ($\gamma = \sqrt{-\beta \cdot \partial_X (\bar{p}_e + \bar{p}_i) / \bar{n}}$), are shown in Fig. 6(b). The instability is saturated as the shearing rate converges to the growth rate; the magnitude of the (positive) maximum of ξ_E, located near the separatrix, increases while the magnitude of the (negative) minimum of ξ_E, located in the near-SOL, decreases to meet γ.

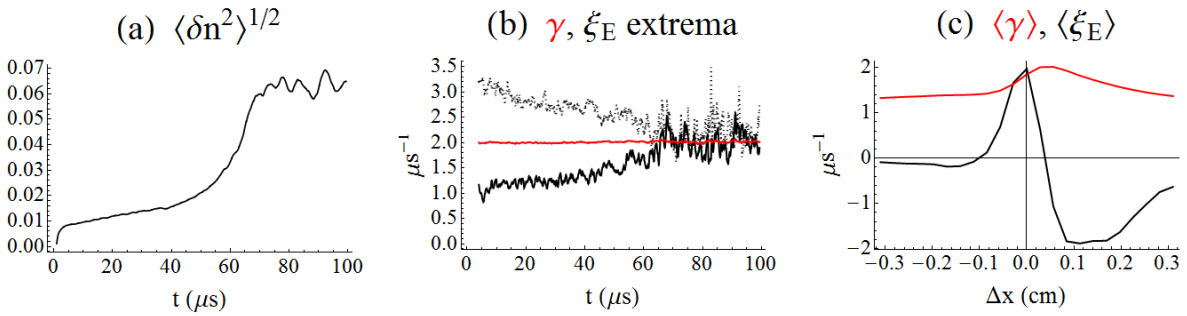

Fig. 6. For the simulation with D_n = 0.17 m^2/sec, starting from small-amplitude noise: (a) the density fluctuation (normalized to the separatrix value) versus time; (b) the maximum value of the interchange growth rate, $\gamma = \sqrt{-\beta \cdot \partial_x (\bar{p}_e + \bar{p}_i) / \bar{n}}$ (red), the maximum value of the shearing rate of the mean ExB flow, $\xi_E = \partial_x \bar{v}_E$ (black), and the magnitude of the minimum value of ξ_E (black dotted) versus time; (c) the time-average of the growth rate and of the shearing rate, over the last 20 μs in (b), versus Δx. In (a), the angular brackets denote the spatial average over the simulation box. In (b), the extrema of ξ_E and the maximum of γ are located within |Δx| < 3 mm, but are not coincident, as seen in (c).

The time- and x-averages of $|\xi_E|$ and γ for all of the simulations are plotted in Fig. 7 versus the density diffusion coefficient. The averages were taken over a ±3 mm neighborhood of the separatrix that included the turbulence generation region (birth zone) and excluded the strongest ballistic (streamer) dynamics farther out in the SOL. It is necessary to average over a neighborhood of the birth zone because the stabilization mechanism acts on a radially extended eigenfunction (the fastest growing mode) and not just at one point. In fact, the time-averaged shearing rate passes through zero approximately where the time-averaged growth rate is maximized, as seen in Fig. 6(c).

The error bars in Fig. 7 are standard deviations with respect to the x-average, within ±3 mm of the separatrix. Thus the mean interchange growth rate is within one standard deviation of the mean flow shearing rate in the turbulence-generation region in all cases. Thus the development of sheared flows appears to play a role in the nonlinear *saturation* of the mode, even in the weak-turbulence case (D_n = 0.23 m^2/sec), but the relationship of sheared flows to turbulent *transport* in a shot-to-shot comparison remains to be elucidated. Additionally, the net effect of *local* shear on these radially *extended* modes can be subtle.

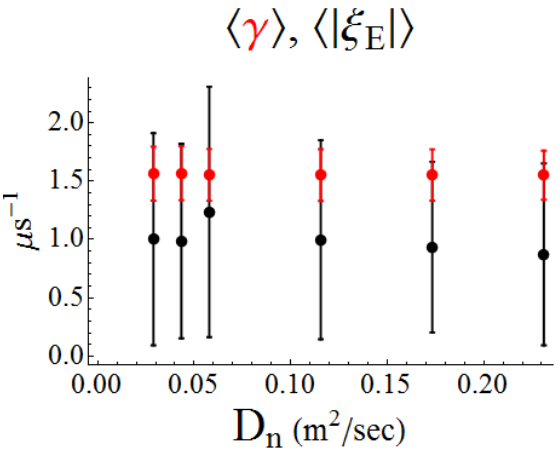

Fig. 7. Time- and x-averages of the interchange growth rate, $\langle \gamma \rangle$ (red), and of the ExB flow shearing rate, $\langle \xi_E \rangle$ (black), versus the density diffusion coefficient D_n. The x-average is restricted to a ±3 mm neighborhood of the separatrix, and the time-average is taken over times long compared to the fluctuation time scale in equilibrium in each case. The error bars are standard deviations with respect to the x-average.

B. Stabilization by wave-breaking and profile modification

Wave-breaking occurs as the turbulent radial velocity fluctuations approach the radial phase velocity of the dominant linear mode driving those fluctuations, in a frame moving with the local ExB drift velocity, viz.,

$$WB \equiv \left| \frac{\delta v_x k_x}{(\omega - k_y v_E)} \right| \sim 1 \qquad (7)$$

Although identifying the underlying linear mode in the saturated turbulent state can prove challenging, it is relatively straightforward in the weak-turbulence case.

In the weak-turbulence case (D_n = 0.23 m^2/sec), there are several isolated local maxima in the density fluctuation energy spectra shown in Fig. 8. Though this case is not directly relevant to the experimental discharge, it provides a relatively unambiguous illustration of the methodology for diagnosing wave-breaking and profile modification in that regime of stronger turbulence.

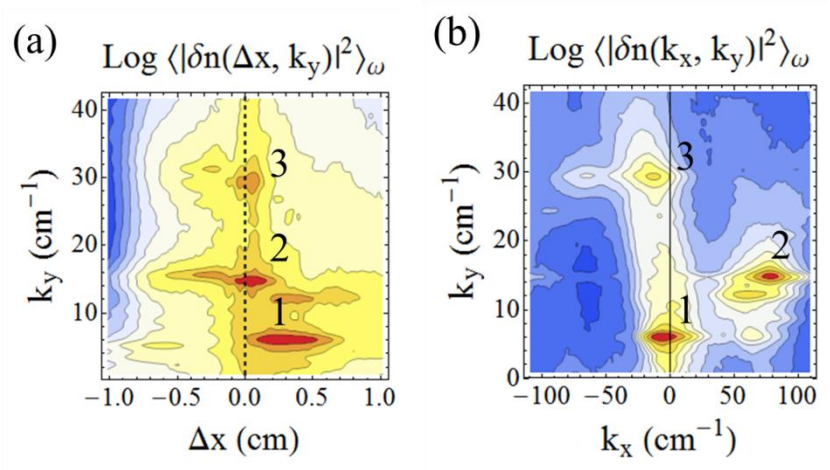

Fig. 8. Energy spectra of the density fluctuations from the weak-turbulence simulation, D_n = 0.23 m^2/sec. The frequency-averaged spectrum is plotted as a function of (Δx, k_y) in (a) and as a function of (k_x, k_y) in (b). Three prominent maxima (or waves), labeled, are discussed in the text. Wave (2) corresponds to the separatrix-spanning interchange mode in Fig. 4(a) and drives the turbulence in the near-SOL.

Wave (1), in Fig. 8, is a long-wavelength feature that extends from the near-SOL into the mid-SOL, corresponding to the rippled red streaks evident in Fig. 3(a). Waves (2) and (3) are localized at about Δx = 1 mm in the near-SOL, as seen in Fig. 8(a). Wave (3) is a harmonic of wave (2), i.e., $\omega_3 = 2\omega_2$ and $k_{y3} = 2k_{y2}$, and so appears to be a weak nonlinear beat-wave product of wave (2) with itself. Both waves lie on the v_{ph} ledge that spans the separatrix in Fig. 4(a). Waves (2) and (3) underly the ubiquitous ripples in the SOL in Fig. 3(a). With decreasing D_n, wave (1) is identified with the streamers and blobs in the strong-turbulence cases, so it appears to be the result of fluctuations propagating into the sheath-dominated mid-SOL from the edge. Thus, waves (1) and (3) likely are products of wave (2). Furthermore, the r.m.s. radial velocity fluctuation profile, $\left\langle (\delta v_x)^2 \right\rangle^{1/2}$, has a narrow global maximum where the interchange growth rate (Fig. 6(c)) is maximized. These features suggest that wave (2) be identified as the dominant mode driving the turbulence in this case.

The wave-breaking parameter, WB (Eq. 7), for wave (2) is calculated as follows. First we specify a radial locaton, Δx_0, for the mode and locate the maximum in the power spectrum of density (or potential) fluctuations, $\left|\delta n(\Delta x_0, k_y, \omega)\right|^2$. In this weak-turbulence case the choice of Δx_0 is obvious: we take the location of maximum interchange growth rate (or minimum density gradient scale length, L_n), i.e., Δx_0 = 0.6 mm, clearly within the body of wave (2) in Fig. 8(a).

The power spectrum (of which Fig. 8(a) depicts the average over ω) has a pronounced maximum at $\omega_0 / k_{y0} = 0.75\ \mathrm{km/sec}$, identifying wave (2) as the separatrix-spanning interchange mode in Fig. 4(a). Next, rather than finding k_x from the *global* energy spectrum, Fig. 8(b), we take it to be the radial gradient of the phase of the potential fluctuation at Δx_0, viz.,

$$k_X = \mathrm{Im}(\delta\phi(\Delta x, k_y, \omega) * \partial_x \delta\phi(\Delta x, k_y, \omega) / \left|\delta\phi(x, k_y, \omega)\right|^2),$$

with the corresponding *local* radial velocity fluctuation $\delta v_X = -ik_y \delta\phi(\Delta x, k_y, \omega)$, both evaluated at ($\Delta x_0$, k_{y0}, ω_0). We find k_x = 27.5 cm^{-1} (versus the 80 cm^{-1} that would be inferred from Fig. 8(b)), $\left|\delta v_X\right| = 0.32\ \mathrm{km/sec}$ and WB = 0.49. We conclude that wave-breaking cannot be ruled out as a saturation mechanism in the weak-turbulence simulation.

Profile-modification is active as a saturation mechanism where the radial gradient of the pressure fluctuation is comparable to the gradient of the profile, which drives the interchange instability, and so acts locally to lower the overall growth rate.,[21] viz.,

$$\mathrm{PM} \equiv \frac{\delta n}{n} L_n \left|k_x\right| \sim 1, \qquad (8)$$

where L_n is the (minimum) gradient scale length of the density profile $L_n^{-1} = -\partial_x \log\langle n\rangle$, "$\delta n / n$" is abbreviation for $\left\langle (\delta n)^2 \right\rangle^{1/2} / \langle n \rangle$, and the angular brackets denote an average over both y and t. In the weak-turbulence simulation, we find PM = 0.19 for wave (2) of Fig. 8 and conclude that profile modification is likely active as a saturation mechanism in the weak-turbulence simulation.

It is not surprising that *both* wave-breaking and profile modification are active in the weak-turbulence simulation because the two mechanisms are closely related.[21] Upon linearizing the density evolution equation (2), about the zero-order fields $\langle n \rangle$ and v_E, and ignoring the sheath and drift-wave terms for simplicity, we find

$$\left| \frac{\delta n}{\nabla_x \langle n \rangle} k_x \right| = \left| \frac{\delta v_x k_x}{(\omega - k_y v_E) + i D_n (k_y^2 + k_x^2)} \right|. \qquad (9)$$

It follows from this expression that PM = WB where $\left|(\omega - k_y v_E)\right| \gg D_n (k_y^2 + k_x^2)$, i.e., where convection dominates diffusion (and sheath and drift-wave physics are ignorable). Otherwise PM < WB is to be expected, as found for the weak-turbulence simulation which has the largest value of D_n.

With decreasing D_n, the fluctuation spectra broaden, and the few waves, apparent in the weak-turbulence case, grow indistinct. In particular, there is no clear choice of unique radial location Δx_0, corresponding to wave (2), at which to measure WB and PM in the other, stronger-turbulence, simulations. However, to serve as saturation mechanisms both processes must act in a neighborhood of the maximum instability growth rate. So we conduct the analysis described above for the singular location (Δx_0) but here throughout the radial interval $|\Delta x| < 3$ mm, and average WB and PM over that interval for each simulation. The result is shown in Fig. 9. The error bars (standard deviations) in the figure indicate the variation of the parameters on the chosen interval and are *sensitive* to that choice. In particular, the off-scale error bar in WB at D_n = 0.116 m^2/sec is due to a Doppler resonance $(\omega - k_y v_E = 0)$ near the SOL-side boundary of the

interval. (A more rigorous analysis would account for turbulent decorrelation to provide a resonance width.) Such qualifications notwithstanding, we conclude from the order-of-magnitude criteria WB ~ 1 and PM ~ 1 (with unknown order unity factors) that wave-breaking and profile modification cannot confidently be ruled out as saturation mechanisms in any of the simulations, although their canonical measures are technically smaller than unity in Fig. 9.

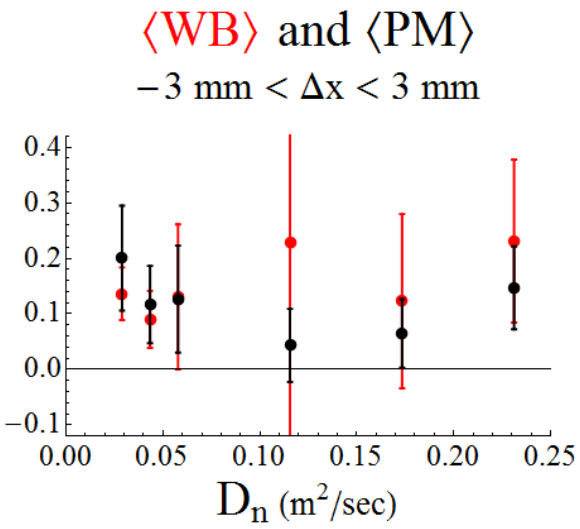

Fig. 9. Wave-breaking (WB, red) and profile modification (PM, black) parameters, Eqs. 7 and 8 respectively, averaged over the radial interval $|\Delta x| < 3$ mm versus the density diffusion coefficient D_n. Error bars are standard deviations with respect to the average.

V. Concluding remarks

We have explored the relationship between blob velocities and mean flow velocities in the edge region of an L-mode discharge on Alcator C-Mod by conducting two-dimensional SOLT simulations. The simulated turbulence was driven by the plasma pressure gradient associated with the density and temperature profiles obtained by smoothly fitting Thomson scattering and MLP data from the discharge. The amplitude of the fluctuations was adjusted by varying the density diffusion coefficient in the simulations until density fluctuation amplitudes were consistent with those measured by MLP in the experiment.

In the simulations, the density fluctuations served as a proxy for neutral emission intensity measured by GPI in the experiment, and blob velocities in the simulations were determined by time-delay estimation (TDE) analysis based on the correlation function for density fluctuations. The simulation velocity profiles were compared with those determined by four different measurement methods applied to the discharge: 1) TDE analysis of GPI emission recorded by an avalanche photo-diode (APD) array, 2) Fourier analysis (FA) of GPI emission recorded by the APD array, 3) FA of GPI emission recorded by a fast-framing Phantom camera, and 4) 2-point phase-delay analysis of fluctuations measured by the MLP. GPI and MLP poloidal velocity profiles were aligned by exploiting their common features. This alignment was necessary to enable a fair comparison between blob velocity profiles in experiment and simulation since the simulation was driven by profiles based on the MLP data.

The agreement, highlighted in Fig. 5, qualitatively captured trends in radial variation. Quantitatively the simulations reproduced measured radial and poloidal turbulence velocities in the SOL to essentially the size of discrepancies between different diagnostics; agreement in the

closed surface region was less spectacular showing deviations of about a factor of two to three from available measurements. In the *simulation*, it was found that these relatively large fluctuations moved poloidally with v_E in the near-SOL.

The agreement between the poloidal velocities measured by APD/TDE in the experiment and in the simulation is subject to the qualification that both were restricted (by the method of analysis or, in the case of the simulation, limited run time) to fluctuations with frequencies greater than 10 kHz. Measurements that included longer time-scale fluctuations could, in principle, find different results.

Larger- D_n, weaker-turbulence simulations, not directly relevant to the C-Mod discharge, were conducted to provide perspective on the stronger turbulence results and to facilitate exploration of saturation mechanisms possibly at work in the simulations. With increasing D_n, the larger, discharge-relevant blobs are transformed progressively into radial streamers and ultimately into weak-turbulence fluctuations characterized by narrow power spectra supported by relatively few waves. In the weak-turbulence regime, it was found that the interchange mode, with group velocity $v_E + 1/2\ v_{di}$ and eigenfunctions localized on radial zones, dominated the blob motion; weak-turbulence blobs move poloidally with the group velocity of this mode throughout the simulation domain, and the ion pressure plays a crucial role in determining that velocity. In the stronger, blobby simulation corresponding to the discharge, the group velocity of the interchange mode is relatively irrelevant to the blob motion.

E×B flow shear and wave-breaking (or profile modification) were explored as possible instability saturation mechanisms in the simulations. It was found that sheared flow stabilization was likely acting in all simulations and that its stabilizing effect was distributed over a radial

interval that included the location of the maximum interchange growth rate, consistent with the radial localization of the interchange mode that was most clearly observed in the weak-turbulence regime. Wave-breaking, closely related to profile modification, was documented in the weak-turbulence case by conducting a radially localized analysis of a single wave, the interchange mode, that dominated the power spectra of fluctuations at the location of maximum growth rate in that case and was argued to be driving the turbulence. For the simulations of stronger turbulence, where broader power spectra challenge methodology based on a single wave, the local analysis was nevertheless applied over a radial interval that included the growth rate maximum, and the wave-breaking and profile modification parameters were averaged over that interval. These parameters were judged to be large enough that wave-breaking and profile modification could not be ruled out as saturation mechanisms in any of the simulations. However, the *relative* roles of stabilization by sheared flow and wave-breaking remain to be determined.

Acknowledgements

This material is based upon work supported by the U.S. Department of Energy Office of Science, Office of Fusion Energy Sciences, under Princeton Plasma Physics Laboratory Subcontract S013429-U, Grant DE-FG02-97ER54392, Agreement DE-FC02-99ER54512, and Contract DE-AC02-09CH11466.

References

[1] K. H. Burrell, Phys. Plasmas **4**, 1499 (1997).

[2] P. W. Terry, Rev. Modern Phys., **72**, 109 (2000).

[3] G.S. Xu, H.Q. Wang, M. Xu, B.N. Wan, H.Y. Guo, P.H. Diamond, G.R. Tynan, R. Chen, N. Yan, D.F. Kong et al., Nucl. Fusion **54**, 103002 (2014).

[4] I. Cziegler, G.R. Tynan, P.H. Diamond, A.E. Hubbard, J.W. Hughes, J. Irby and J.L. Terry, Nucl. Fusion **55**, 083007 (2015).

[5] L. Schmitz, L. Zeng, T.L. Rhodes, J.C. Hillesheim, W.A. Peebles, R.J. Groebner, K.H. Burrell, G.R. McKee, Z. Yan, G.R. Tynan, P.H. Diamond, J.A. Boedo, E.J. Doyle, B.A. Grierson, C. Chrystal, M.E. Austin, W.M. Solomon and G. Wang, Nucl. Fusion **54**, 073012 (2014).

[6] X. Q. Xu, R. H. Cohen, T. D. Rognlien, and J. R. Myra, Phys. Plasmas **7**, 1951 (2000).

[7] K. Miki, P. H. Diamond, S.-H. Hahn, W.W. Xiao, O. D. Gürcan, and G. R. Tynan, Phys. Rev. Lett. **110**, 195002 (2013).

[8] L. Chôné, P. Beyer, Y. Sarazin, G. Fuhr, C. Bourdelle and S. Benkadda, Nucl. Fusion **55**, 073010 (2015).

[9] G. Y. Park, S. S. Kim, H. Jhang, P. H. Diamond, T. Rhee, and X. Q. Xu, Phys. Plasmas **22**, 032505 (2015).

[10] C. Bourdelle, C.F. Maggi, L. Chôné, P. Beyer, J. Citrin, N. Fedorczak, X. Garbet, A. Loarte, F. Millitello, M. Romanelli, Y. Sarazin and JET EFDA Contributors, Nucl. Fusion **54**, 022001 (2014).

[11] G. M. Staebler and R. J. Groebner, Plasma Phys. Control. Fusion **57**, 014025 (2015).

[12] P. Ricci and B. N. Rogers, Phys. Plasmas 20, 010702 (2013).

[13] A. Mosetto, F. D. Halpern, S. Jolliet, J. Loizu and P. Ricci, Phys. Plasmas **20**, 092308 (2013).

[14] J. R. Myra, D. A. Russell, D. A. D'Ippolito, J.-W. Ahn, R. Maingi, R. J. Maqueda, D. P. Lundberg, D. P. Stotler, S. J. Zweben, J. Boedo, M. Umansky, and NSTX Team, Phys. Plasmas **18**, 012305 (2011).

[15] D. A. Russell, D. A. D'Ippolito, J. R. Myra, B. LaBombard, J. L. Terry, and S. J. Zweben, Phys. Plasmas **19**, 082311 (2012).

[16] F. Militello, V. Naulin, and A. H. Nielsen, Plasma Phys. Controlled Fusion **55**, 074010 (2013).

[17] D. A. Russell, D. A. D'Ippolito, J. R. Myra, J. M. Canik, T. K. Gray, and S. J. Zweben, Phys. Plasmas **22**, 092311 (2015).

[18] F. D. Halpern, P. Ricci, B. Labit, I. Furno, S. Jolliet, J. Loizu, A. Mosetto, G. Arnoux, J. P. Gunn, J. Horacek, M. Kocan, B. LaBombard, C. Silva, and JET-EFDA, Nucl. Fusion **53**, 122001 (2013).

[19] F. D. Halpern, P. Ricci, S. Jolliet, J. Loizu, and A. Mosetto, Nucl. Fusion **54**, 043003 (2014).

[20] J. Loizu, P. Ricci, F. D. Halpern, S. Jolliet, and A. Mosetto, Nucl. Fusion **54**, 083033 (2014).

[21] J. R. Myra, D. A. D'Ippolito, and D. A. Russell, Phys. Plasmas **22**, 042516 (2015).

[22] S. J. Zweben, J. L. Terry, M. Agostini, W. M. Davis, A. Diallo, R. A. Ellis,T. Golfinopoulos, O. Grulke, J. W. Hughes, B. LaBombard, M. Landreman, J. R. Myra, D. C. Pace, and D. P. Stotler, Phys. Plasmas **20**, 072503 (2013)..

[23] J. A. Boedo, J. R. Myra, S. Zweben, R. Maingi, R. J. Maqueda, V. A. Soukhanovskii, J. W. Ahn, J. Canik, N. Crocker, D. A. D'Ippolito, R. Bell, H. Kugel, B. Leblanc, L. A. Roquemore, D. L. Rudakov, and NSTX Team, Phys. Plasmas **21**, 042309 (2014).

[24] B. LaBombard, T. Golfinopoulos, J. L. Terry, D. Brunner, E. Davis, M. Greenwald, J. W. Hughes, and Alcator CMod Team, Phys. Plasmas **21**, 056108 (2014).

[25] S. J. Zweben, R. J. Maqueda, D. P. Stotler, A. Keesee, J. Boedo, C. E. Bush, S. M. Kaye, B. LeBlanc, J. L. Lowrance, V. J. Mastrocola, R. Maingi, N. Nishino, G. Renda, D. W. Swain, J. B. Wilgen, and NSTX Team, Nucl. Fusion 44, 134 (2004).

[26] J. L. Terry, S. J. Zweben, K. Hallatschek, B. LaBombard, R. J. Maqueda, B. Bai, C. J. Boswell, M. Greenwald, D. Kopon, W. M. Nevins, C. S. Pitcher, B. N. Rogers, D. P. Stotler, and X. Q. Xu, Phys. Plasmas 10, 1739 (2003).

[27] N. Fedorczak, P. Manz, S. C. Thakur, M. Xu, G. R. Tynan, G. S. Xu, and S. C. Liu, Phys. Plasmas **19**, 122302 (2012).

[28] I. Cziegler, G. R. Tynan, P. H. Diamond, A. E. Hubbard, J. W. Hughes, J. Irby and J. L. Terry, Plasma Phys. Control. Fusion **56**, 075013 (2014).

[29] I. Cziegler, J. L. Terry, J. W. Hughes, and B. LaBombard, Phys. Plasmas **17**, 056120 (2010).

[30] W.M. Davis, M.K. Ko, R.J. Maqueda, A.L. Roquemore, F. Scotti, S.J. Zweben, Fusion Eng. Des. **89**, 717 (2014).

[31] T. Munsat and S. J. Zweben, Rev. Sci. Instrum. **77**, 103501 (2006).

[32] J. M. Sierchio, I. Cziegler, J. L. Terry, A. E. White, and S. J. Zweben, to be published in Rev. Sci. Instrum. (2016).

[33] S. I. Krasheninnikov, D. A. D'Ippolito and J. R. Myra, J. Plasma Physics **74**, 679 (2008).

[34] D. A. D'Ippolito, J. R. Myra, and S. J. Zweben, Phys. Plasmas **18**, 060501 (2011).

[35] M. Greenwald, A. Bader, S. Baek, M. Bakhtiari, H. Barnard, W. Beck, W. Bergerson, I. Bespamyatnov, P. Bonoli, D. Brower,et al., Phys. Plasmas **21**, 110501 (2014).

[36] D. A. Russell, J. R. Myra, and D. A. D'Ippolito, Phys. Plasmas **16**, 122304 (2009).

[37] G. Q. Yu, S. I. Krasheninnikov, and P. N. Guzdar, Phys. Plasmas 13, 042508 (2006).

[38] G. Birkenmeier, F. M. Laggner, M. Willensdorfer, T. Kobayashi, P. Manz, E. Wolfrum, D. Carralero, R. Fischer, B. Sieglin, G. Fuchert, U. Stroth and the ASDEX upgrade team, Plasma Phys. Control. Fusion **56**, 075019 (2014).

[39] P. Manz, G. Birkenmeier, D. Carralero, G. Fuchert, H. W. Müller, S. H. Müller, B. D. Scott, U. Stroth, T. T. Ribeiro, E. Wolfrum and the ASDEX Upgrade Team, Plasma Phys. Control. Fusion **57**, 014012 (2015).

[40] D. Jovanovic, P. K. Shukla and F. Pegorano, Phys. Plasmas **15**, 112305 (2008).

[41] J. Madsen, O. E. Garcia, J. S. Larsen, V. Naulin, A. H. Nielsen and J. J. Rasmussen Phys. Plasmas **18**, 112504 (2011).

[42] P. Manz, D. Carralero, G. Birkenmeier, H. W. Müller, S. H. Müller, G. Fuchert, B. D. Scott, and U. Stroth, Physics of Plasmas **20**, 102307 (2013).

[43] N. Bisai and P. K. Kaw, Phys. Plasmas **20**, 042509 (2013).

[44] M. Wiesenberger, J. Madsen, and A. Kendl, Physics of Plasmas **21**, 092301 (2014).

[45] A. Mosetto, F. D. Halpern, S. Jolliet, J. Loizu, and P. Ricci, Physics of Plasmas **22**, 012308 (2015).

[46] A.N. Simakov and P.J. Catto, Phys. Plasmas **10**, 4744 (2003).

[47] M.V. Umansky, X.Q. Xu, B. Dudson, L.L. LoDestro and J.R. Myra, Comp. Phys. Comm. **180**, 887 (2009).

[48] J.R. Angus, S.I. Krasheninnikov and M.V. Umansky, Phys. Plasmas **19**, 082312 (2012).

[49] M.V. Umansky, S.I. Krasheninnikov, B. LaBombard, B. Lipschultz and J.L. Terry, Phys. Plasmas **6**, 2791 (1999).

[50] W.M. Tang and Peter J. Catto, Phys. Fluids **24**, 1314 (1981).

[51] I. Cziegler, J.L. Terry, J.W. Hughes and B. LaBombard, Phys. Plasmas **17**, 056120 (2010).